metals

MDPI

Article

Controllable Synthesis of Flower-like Hierarchical $CuCo_2S_4$ Nanostructure Arrays for High-Performance Hybrid Supercapacitors

Man Li [1], Ningning Yu [1], Lei Xu [1], Wenyu Wang [1], Fuxiang Wei [1,2,*], Jiqiu Qi [1,3] and Yanwei Sui [1,2]

[1] School of Materials and Physics, China University of Mining and Technology, Xuzhou 221116, China; lm1417514487@163.com (M.L.); 18037512516@163.com (N.Y.); jskxl7@163.com (L.X.); wvy21180049@163.com (W.W.); flower_cumt@outlook.com (J.Q.); wyds123456@outlook.com (Y.S.)
[2] Jiangsu Huaihai New Energy Co., Ltd., Xuzhou 221006, China
[3] Jiangsu Province Engineering Laboratory of High Efficient Energy Storage Technology and Equipments, China University of Mining and Technology, Xuzhou 221116, China
* Correspondence: weifuxiang2001@163.com

Abstract: Transition metal sulfides (TMSs) are considered as attractive materials in the areas of energy storage because of their unique redox properties, excellent electronic conductivity, as well as environmental friendliness. However, poor cyclic stability and limited electrochemical active sites hinder their further application. To address this issue, a flower-like hierarchical $CuCo_2S_4$ structure is constructed by a two-step hydrothermal method. In this nanostructure, $CuCo_2S_4$ grows outward to form a tightly bound hierarchical structure on the nickel foams (NFs). This oriented structure can provide more laminar gaps for electrolyte ion diffusion, exposing more reaction sites to increase the ion transport efficiency between the layers, reducing the ion transport resistance and improving the reaction kinetics. Thus, the $CuCo_2S_4$ electrode exhibits excellent energy storage performance, exhibiting a high specific capacity of 1415.6 F g^{-1} at 1 A g^{-1}. After 10,000 cycles of 10 A g^{-1}, it still has 91.9% of the initial performance. In addition, an asymmetrical supercapacitor (ASC) was constructed by choosing $CuCo_2S_4$ as the anode and RGO as the cathode, which has the maximum energy density (61.8 Wh Kg^{-1}) at 812.1 W Kg^{-1} and significant cycling endurance (92.05% retention) at 10,000 turns. Briefly, the researchers successfully constructed an array of $CuCo_2S_4$ flower-like hierarchical nanostructures and confirmed their potential application in supercapacitors.

Keywords: TMSs; $CuCo_2S_4$; flower-like hierarchical nanostructure; supercapacitor

check for updates

Citation: Li, M.; Yu, N.; Xu, L.; Wang, W.; Wei, F.; Qi, J.; Sui, Y. Controllable Synthesis of Flower-like Hierarchical $CuCo_2S_4$ Nanostructure Arrays for High-Performance Hybrid Supercapacitors. *Metals* **2024**, *14*, 145. https://doi.org/10.3390/met14020145

Academic Editors: Jürgen Eckert and Marcello Cabibbo

Received: 22 December 2023
Revised: 20 January 2024
Accepted: 22 January 2024
Published: 24 January 2024

1. Introduction

The escalating issues of environmental pollution and energy crisis have garnered global attention, prompting researchers to urgently explore efficient, renewable, and clean sources of sustainable energy [1–5]. Supercapacitors (SCs) are expected to be the promising alternatives for next-generation high-performance power supplies due to their fast charging and discharging processes, excellent power density, high cycle life, and high safety [6–11]. Based on the charge storage mechanism, SCs can be classified into two categories [12]: pseudo-capacitors, which utilize Faraday reversible reactions, and electric double-layer capacitors (EDLCs), which involve the accumulation of the electrostatic charges at the electrode/electrolyte interface. However, the relatively low energy density is still the main problem that impedes the large-scale application of SCs. In most cases, the energy density of SCs can be affected by the structure of the electrode materials, such as hollow nanostructures, core-shell structures, and lamellar structures [13]. Several recent studies have reported that optimizing and designing the morphology structure of electrode materials is one of the defining means of raising the energy density of SCs [14–16]. However, the development of high-performance electrode materials to bolster their energy density remains an exceptionally challenging undertaking [17,18].

In the last decades, carbon materials (e.g., porous carbon, graphene, etc.), transition metal oxides (e.g., Co_3O_4, Mn_3O_4), and conductive polymers (e.g., polypyrrole, polyaniline, etc.) have often been used to fabricate pseudocapacitors [19,20]. However, the low performance of activated carbon and the poor thermal stability and cycling performance of conductive polymers have limited the practical application of SCs to some extent [21]. In terms of transition metal oxides, they have higher structural flexibility and excellent specific capacitance, but their slower electron conduction may hinder their practical application in the commercial storage [22]. Transition metal sulfides have more preparation pathways and multiple redox states compared to transition metal oxides and are capable of obtaining more nanostructures, which can effectively promote redox reactions in capacitors. They also have many advantages, such as abundant resources, low cost, and better conductivity, which make them more widely used in SCs. Transition metal sulfides have superior thermal stability and electrical conductivity and higher electrochemical activity than the corresponding transition metal oxides [20,22]. The M-S bonding energy of metal sulfides is lower than the M-O bonding energy of metal oxides, which is more favorable for the electrochemical storage [23]. In addition, compared with binary metal sulfides, polymetallic sulfides have higher electrical conductivity and specific capacitance due to the participation and synergistic effect of multiple cations in redox reactions and the excellent electrochemical activity [24,25]. Further, due to its low electronegativity, sulfur possesses a more flexible structure, which is conducive to improving the electron transport potency. For these reasons, TMSs have attracted extensive attention from researchers as a promising electrode material for SCs [26,27].

Metal sulfides, such as $NiCo_2S_4$ [28], Co_3S_4 [29], and $CuCo_2S_4$ [30], due to their excellent pseudocapacitance properties, have been recognized as a popular research direction for SCs electrode materials in recent years. Among them, $CuCo_2S_4$, in which Cu occupies a tetrahedral position and Co occupies an octahedral position, has attracted special attention owing to its abundant redox state and environmental friendliness [31–33]. However, $CuCo_2S_4$ cannot meet the current demand of SCs due to its limited electrochemical active sites [24,25,34]. In order to solve the problems above, an effective approach is to improve the electrochemical behavior of transition metal sulfides by optimizing morphology and structural engineering strategies [26,35]. The morphology of the electrode material can determine its effective contact area with the electrolyte, thus affecting the electrochemical reaction active sites and charge diffusion paths. For instance, Zhang [23] et al. synthesized three-dimensional hollow nanotube $CuCo_2S_4$ arrays by the solvothermal method, with a specific capacitance of 458.8 C g^{-1} at 1.0 A g^{-1} and a capacity retention of 96% after 1000 consecutive charge/discharge cycles. Fan [36] team prepared a $CuCo_2S_4$ nanosheet array under hydrothermal conditions, possessing a high specific capacitance of 3132.7 F g^{-1} at 1 A g^{-1} and a maximum energy density (46 Wh kg^{-1}) at a power density of 992 W kg^{-1}. Wang [37] et al. synthesized oriented nanograss arrays consisting of $CuCo_2S_4$ nanocrystals by using a hydrothermal method with a retention rate higher than 99% after 5000 cycles and obtained a high energy density of 32 Wh kg^{-1}. Jia et al. [33] prepared hollow sea urchin-like $CuCo_2S_4$ microspheres by using the hydrothermal and vulcanization methods. A high specific capacitance of 1069 F g^{-1} was obtained at 1 A g^{-1}, with 88% capacity retention after 5000 charge/discharge cycles. Although metal sulfides have high electrochemical activity and excellent specific capacity, the electrode materials are subject to phase transition reactions during electrochemical reactions, which cause volume changes in the electrodes, thereby reducing the reaction kinetics, as well as generating harmful side reactions. Therefore, the controlled preparation of $CuCo_2S_4$ with the desired microstructure remains a great challenge.

In this work, flower-like hierarchical $CuCo_2S_4$ nanostructures were synthesized on NFs by a simple two-step solvent heat method with a well-designed structural design strategy. Because of the unique flower-like hierarchical structure, the $CuCo_2S_4$ electrode material significantly enhances the kinetics of ionic reactions. Moreover, the binder-free $CuCo_2S_4$ grown directly on the NFs exhibits good electrical conductivity. With the advantages of

short electron transport distance, fully exposed active sites, and synergistic effects of copper and cobalt, $CuCo_2S_4$ demonstrates excellent cycling stability and multiplicative properties. These findings suggest that the strategy proposed in this work provides a practical and effective method for improving the performance and nanostructure design of SCs.

2. Experimental Section

2.1. Materials

The NFs were purchased from Tianjin Damao Chemical Reagent Co., Ltd. (Tianjin, China) Cobalt nitrate hexahydrate ($Co(No_3)_2{\cdot}6H_2O$), Thioacetamide (TAA), Urea (CH_4N_2O), Copper nitrate trihydrate ($Cu(No_3)_2{\cdot}3H_2O$), and Potassium Hydroxide (KOH) were purchased from the official website of Aladdin Reagent (Shanghai, China), and all of the chemicals were analytically pure and not further purified. The deionized water used came from local sources.

2.2. Synthesis of $(Cu^{+2}, Co)_2(CO_3)(OH)_2$ Nanosheets

The NFs (1×2 cm^{-1}) were washed with 2 M HCl under ultrasonic conditions for 20 min and followed by three repeated washes with ethanol and deionized water (DI), then dried for 6 h. Meanwhile, 0.045 g of $Cu(NO_3)_2{\cdot}3H_2O$, 0.525 g of $Co(NO_3)_2{\cdot}6H_2O$, and 0.565 g of urea were dissolved in 40 mL of DI. The resulting solution was transferred to a 50 mL autoclave, and the NFs were suspended in the center of the solution and reacted at 90 °C for 12 h. The obtained NFs were then washed with DI and ethanol and finally dried under vacuum at 60 °C; this product is marked as Cu-CCO.

2.3. Synthesis of $CuCo_2S_4$

The Cu-CCO obtained previously was put into an autoclave containing a solution of 0.06 mol L^{-1} C_2H_5NS (TAA) and sulfurized at 120 °C for 6 h. The obtained NFs were rinsed with ethanol and DI 3–4 times and then dried under vacuum at 60 °C for 10 h. The final product was labeled as $CuCo_2S_4$-6M. As a control test, the electrode materials with TAA concentrations of 0.05 mol L^{-1} and 0.07 mol L^{-1} were synthesized and labeled as $CuCo_2S_4$-5M and $CuCo_2S_4$-7M, respectively. Furthermore, while keeping the sulfidation concentration constant at 6 M, different reaction times of 5 h, 6 h, and 7 h were used to evaluate the implication of sulfidation time on the properties of $CuCo_2S_4$. These samples were labeled as $CuCo_2S_4$-5h, $CuCo_2S_4$-6h, and $CuCo_2S_4$-7h, respectively.

2.4. Characterization

The morphology and microstructure were characterized by scanning electron microscopy (SEM, SU8010) and transmission electron microscopy (TEM, Tecnai G2 F20 (FEI Company, Hillsboro, OR, USA)). X-ray diffraction (XRD, a Rigaku D/max-2550 PC) tests were carried out to analyze the p crystal structure with Cu Kα radiation. The chemical state of the samples was analyzed using X-ray photoelectron spectroscopy (XPS, ESCALAB 250Xi (ThermoFisher Scientific, Waltham, MA, USA)). Fourier-transform infrared spectroscopy (FT-IR) was performed on a Perkin-Elmer Spectrum One B instrument using the KBr pellet technique.

2.5. Electrochemical Measurements

The CHI 660E electrochemical workstation (CH Instruments, Inc., Bee Cave, TX, USA) was used for cyclic voltammetry (CV), constant current charge/discharge (GCD), and electrochemical impedance spectroscopy (EIS) in the range of 0.01 to 100 kHz. The cyclic stability of the electrodes was tested by a Land cell measurement system (Wuhan Land Electronics Co., Ltd., Wuhan, China) at a current density of 10 A g^{-1}. In the three-electrode system, 2 M KOH was used as the aqueous electrolyte, and $CuCo_2S_4$ was employed as the working electrode, where both the platinum plate and the saturated calomel electrode

(SCE) were used as the counter and reference electrodes. The calculation of specific capacity (C_g (F g^{-1})) is based on GCD curves by the following equation:

$$C_g = \frac{It}{m} \tag{1}$$

where I (A), t (s), and m (g) represent discharge current density, discharge time, and loading mass, respectively.

2.6. Fabrication of Asymmetrical Supercapacitor (ASC)

ASC devices were assembled in 2 M KOH by using reduced graphene oxide and $CuCo_2S_4$ as negative and positive electrodes of ASC, respectively. The negative electrode material was prepared as follows: reduced graphene oxide (RGO), polyvinylidene fluoride (PVDF), and acetylene black were dispersed in N-methylpyrrolidone (NMP) at a mass ratio of 8:1:1 and milled for thirty minutes to form a homogeneous slurry. The slurry was then uniformly applied to the NFs, dried under vacuum at 60 °C for 24 h, and pressed at 10 MPa for 2 min. The mass ratio of the active material between the two electrodes is determined by means of the principle of charge balance (Equations (2) and (3)).

$$Q^+ = Q^- \tag{2}$$

$$\frac{m^+}{m^-} = \frac{I_m^- \times \Delta t}{I_m^+ \times \Delta t} \tag{3}$$

where m^+ and m^- refer to their loadings of active substances (g); I_m^- and I_m^+ are discharge currents of negative and positive electrodes; and both Q^- and Q^+ are stored charges in negative and positive electrodes (C), respectively.

3. Results and Discussion

The synthesis process of flower-like hierarchical $CuCo_2S_4$ nanostructure arrays is shown in Figure 1. First, Cu-CCO precursor nanosheets were grown in NFs substrates by use of simple solvent methods (Figure S2). Then, the prepared Cu-CCO precursor was immersed in TAA solution via a secondary hydrothermal method and stored at 120 °C for 6 h. $CuCo_2S_4$ arrays with flower-like hierarchical nanostructure were obtained through ion etching and exchange.

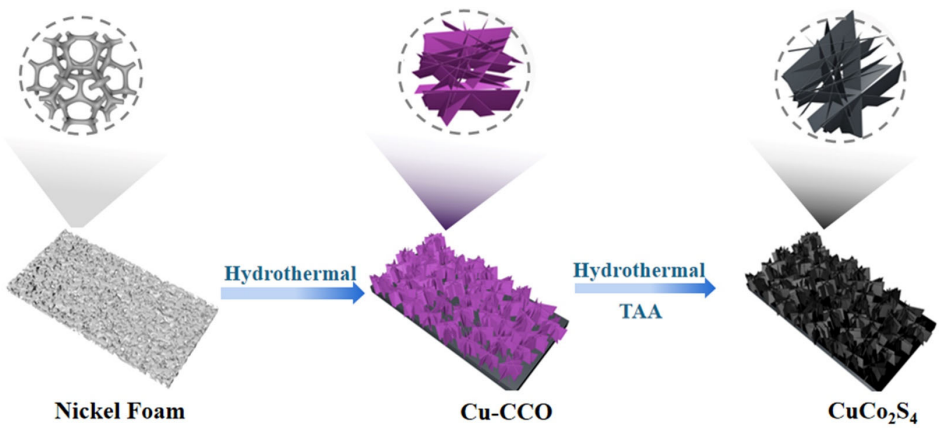

Figure 1. Flow chart for the synthesis of $CuCo_2S_4$.

XRD tests were performed on $CuCo_2S_4$, as shown in Figure 2a,b. Among them, the diffraction peaks at positions 44.4°, 51.7°, and 76.3°are from the nickel foam substrate [38]. As shown in Figure 2a, all the peaks of $CuCo_2S_4$ obtained after the vulcanization of Cu-CCO in the presence of TAA match exactly with the standard card (JCPDS no.42-1450) [39]. The diffraction peaks at 2θ of 54.83°, 50.01°, 46.15°, 38.13°, and 31.27° are attributed to the (044),

(115), (224), (004), and (113) crystal planes of the $CuCo_2S_4$ phase, respectively. A weak diffraction peak can be seen at 22.1° when the TAA concentration is 0.07 M. This is due to the reaction of S^{2-} with the NFs substrate, forming Ni_3S_2 when the sulfide concentration is too high [40]. In Figure 2b, all the peaks of $CuCo_2S_4$ correspond well to the peaks of the standard card. In addition, no other impurity peaks in the XRD spectra indicates that there is no growth of other impurity elements on the surface of NFs.

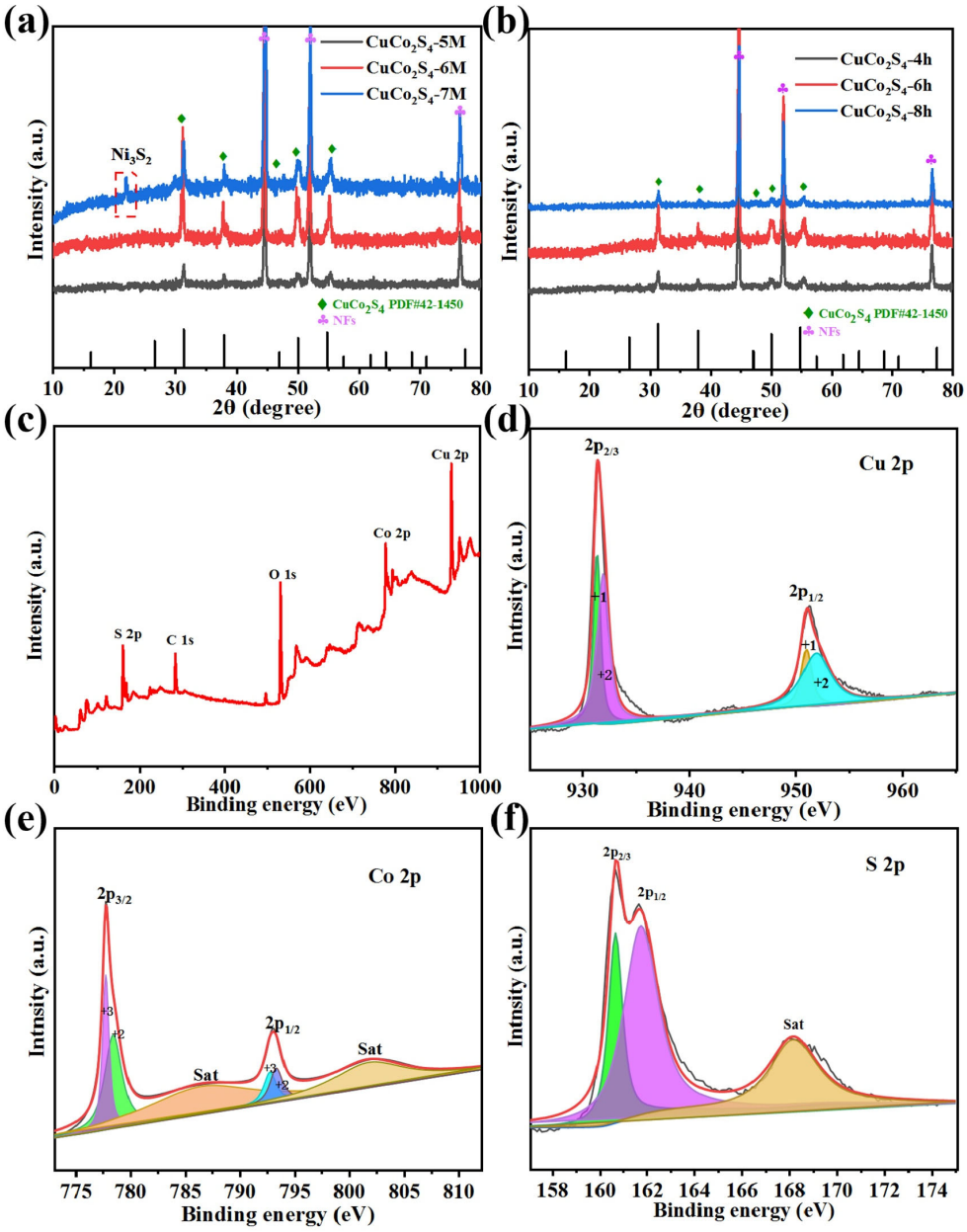

Figure 2. (**a**) XRD diagram of $CuCo_2S_4$-5M, $CuCo_2S_4$-6M, and $CuCo_2S_4$-7M; (**b**) XRD patterns of $CuCo_2S_4$-4h, $CuCo_2S_4$-6h, and $CuCo_2S_4$-8h; (**c**) XPS full spectrum of $CuCo_2S_4$-6h, (**d**) Cu 2p, (**e**) Co 2p, and (**f**) S 2p.

The chemical state and chemical structure of $CuCo_2S_4$ were tested using XPS. The full XPS spectrum of Figure 2c contains Cu, Co, and S elements, which is consistent with the XRD results, indicating the successful synthesis of $CuCo_2S_4$. The Cu 2p spectrum in Figure 2d exhibits the $2p_{2/3}$ and $2p_{1/2}$ orbitals of Cu, with two peaks observed at 933.7 and 955.2 eV. In parallel, the Cu 2p spectra reveal two peaks for Cu^+ at 932.1 and 952.0 eV, as well as two peaks for Cu^{2+} at 955.6 and 935 eV, suggesting the coexistence of Cu^+

and Cu^{2+} [41,42]. As depicted in Figure 2e, in the high-resolution spectrum of Co 2p, the two peaks at 797.2 and 781.6 eV can be observed, corresponding to the $2p_{1/2}$ and $2p_{2/3}$ orbitals of Co. Additionally, the peaks at 780.6 eV (Co $2p_{3/2}$) and 796.4 eV (Co $2p_{1/2}$) are attributed to Co^{2+}, while the peaks at 778.5 eV (Co $2p_{3/2}$) and 793.5 eV (Co $2p_{1/2}$) indicate the presence of Co^{3+}, suggesting the existence of Co^{3+} and Co^{2+} [43]. Figure 2f displays the spectrum of S 2p, which exhibits two peaks around 161.7 and 162.8 eV, belonging to S $2p_{3/2}$ and S $2p_{1/2}$, respectively [44].

Figure 3a,b illustrate the flower-like hierarchical $CuCo_2S_4$-5M nanostructures uniformly dispersed on the NFs. Figure 3c,d exhibit SEM images of $CuCo_2S_4$-6M at varying magnifications. The SEM image in Figure 3d reveals the intricate flower-like hierarchical nanostructures. At lower magnification in Figure 3c, it is evident that the nanoflower is a stack of nanosheets with a thickness of approximately 50–60 nm. These nanosheets intersect with each other, forming a multilayer structure that provides ample space and facilitates the diffusion of electrolyte ions. Figure 3e,f show the microscopic morphology of $CuCo_2S_4$-7M. It can be observed that an excessively high concentration of TAA etching destroys the morphology of flower-like hierarchical $CuCo_2S_4$ nanostructures, resulting in their accumulations and agglomerations on the NFs.

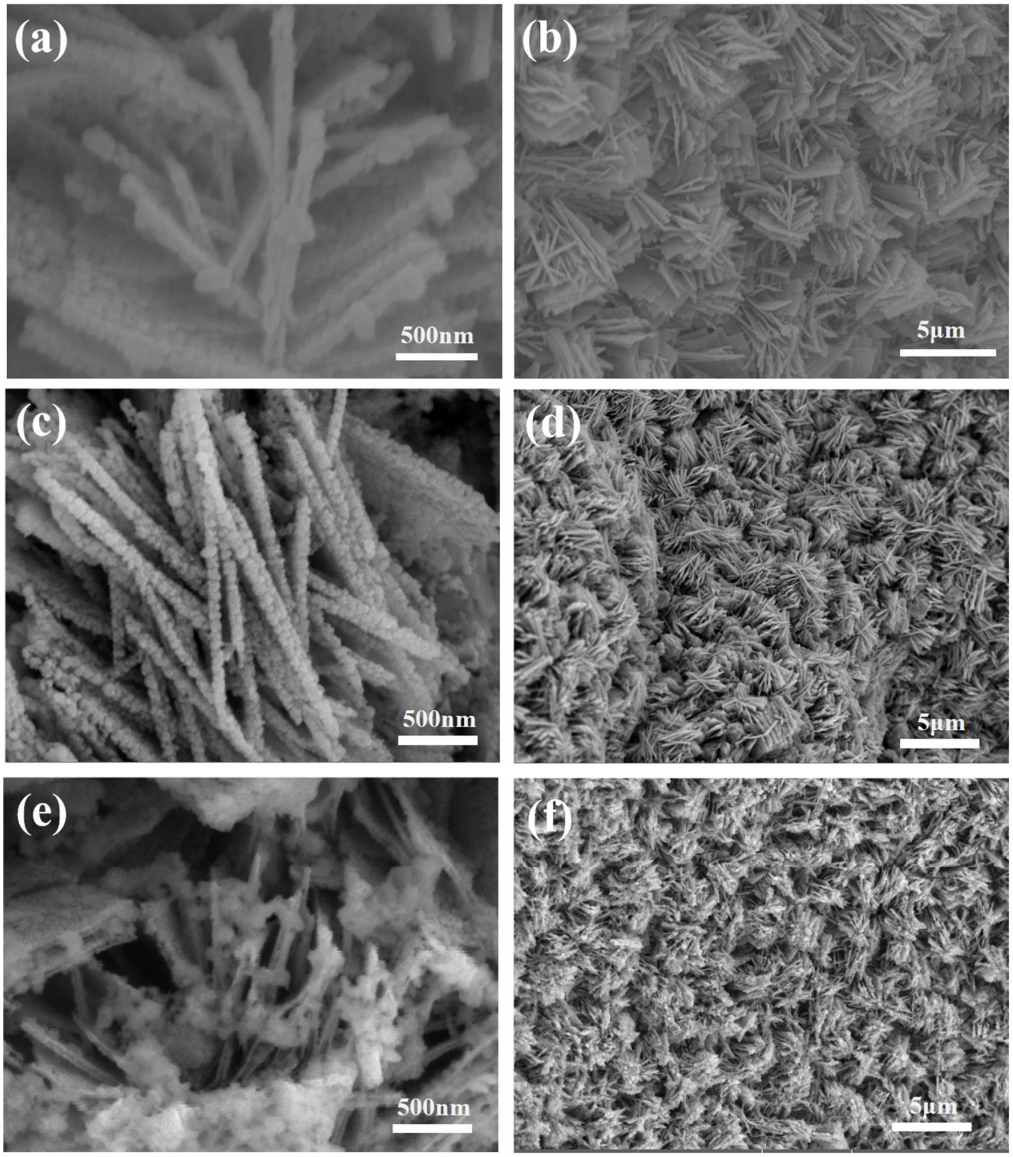

Figure 3. SEM images of (**a**,**b**) $CuCo_2S_4$-5M; (**c**,**d**) $CuCo_2S_4$-6M; (**e**,**f**) $CuCo_2S_4$-7M.

In order to investigate the optimal time for vulcanization, this study also explores the effect of hydrothermal time on the morphology of the material after vulcanization. It is worth noting that even after further sulfuration treatment, the Cu-CCO precursor was successfully converted to $CuCo_2S_4$, while maintaining its flower-like hierarchical nanostructures (Figure 4a,b). As shown in the SEM images captured after a hydrothermal time of 6 h in Figure 4c,d, the flower-like hierarchical $CuCo_2S_4$ nanostructure arrays grown on the NFs are more upright and ordered; the electrodes have more contact with the electrolyte, thus providing more active reaction sites. On the other hand, as shown in Figure 4e,f, the vertically grown flower-like hierarchical nanostructures on NFs appear less ordered and structurally intact compared with $CuCo_2S_4$-6h.

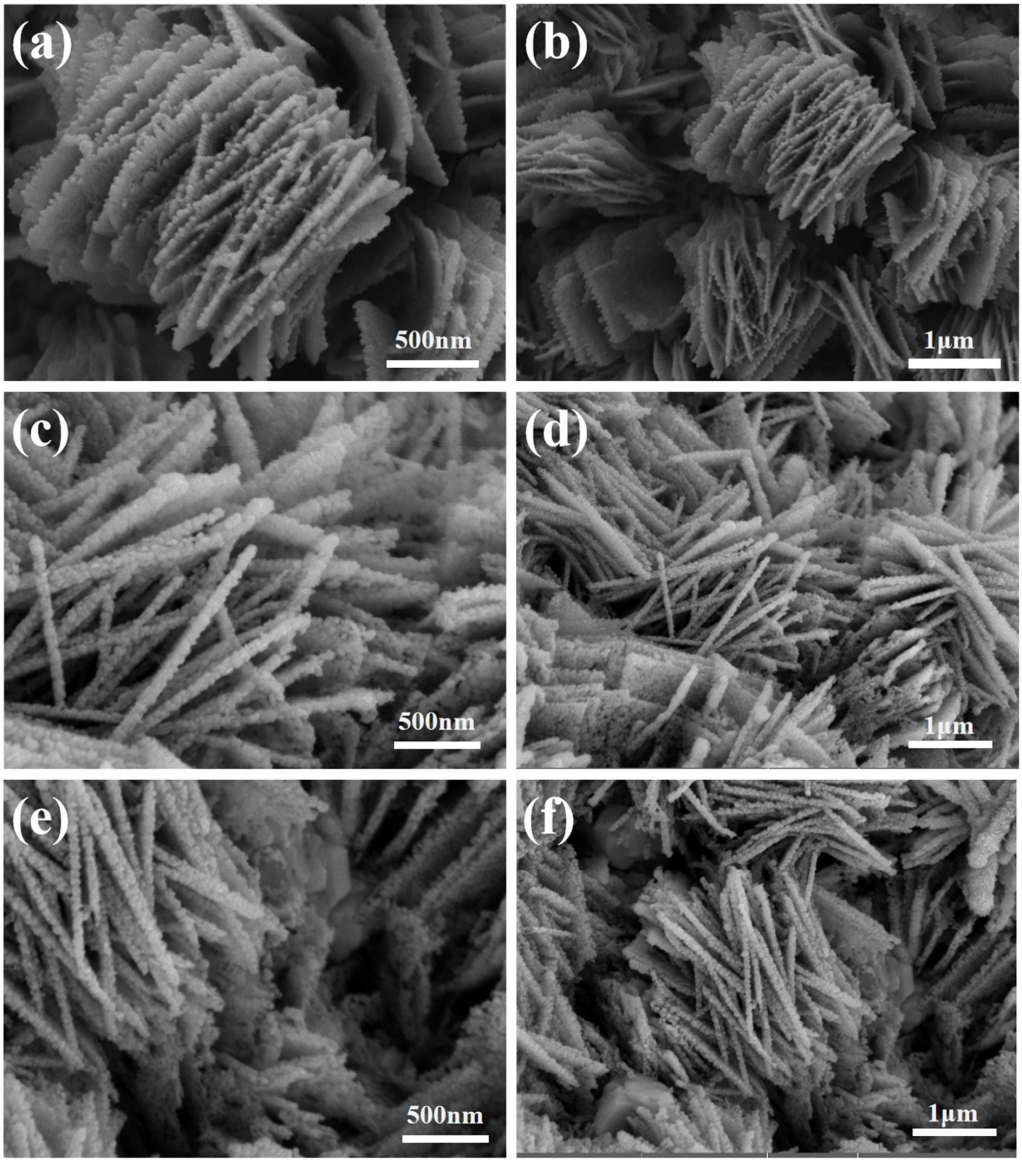

Figure 4. SEM images of (**a**,**b**) $CuCo_2S_4$-4h; (**c**,**d**) $CuCo_2S_4$-6h; (**e**,**f**) $CuCo_2S_4$-8h.

To further observe the microstructure and crystallinity of $CuCo_2S_4$, it was analyzed using TEM. Figure 5a shows a high-magnification scanning transmission electron micrograph of $CuCo_2S_4$, and the facet spacing of 0.33 nm and 0.28 nm obtained from the TEM maps corresponds to the (133) and (022) facets of the $CuCo_2S_4$ spinel phase [45]. Figure 5b displays the selected electron diffraction map of $CuCo_2S_4$, where diffraction rings correspond to the (022), (224), and (004) crystal planes of $CuCo_2S_4$. These findings align with the

results obtained from the XRD. The elemental mapping of $CuCo_2S_4$-6M (Figure 5c) shows that Cu, Co, and S elements are uniformly distributed in the sample.

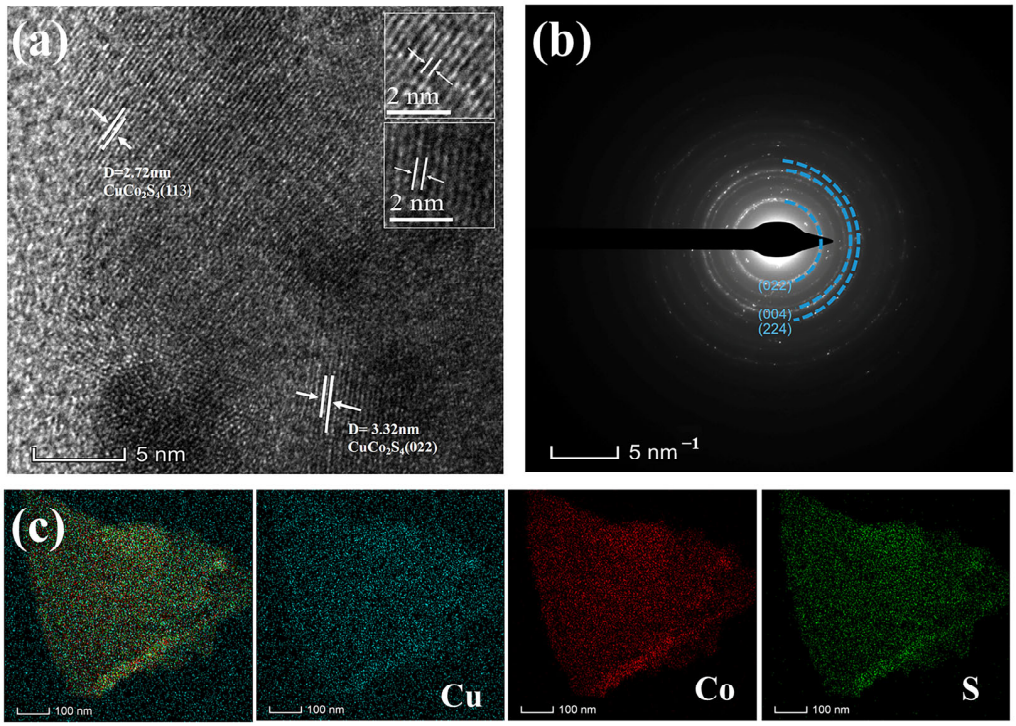

Figure 5. (**a**) HRTEM images of $CuCo_2S_4$, (**b**) SAED pattern of $CuCo_2S_4$, (**c**) Elements mapping images of $CuCo_2S_4$.

The electrochemical performance of $CuCo_2S_4$ was evaluated using a three-electrode system, including CV, GCD, and EIS tests. To further understand the relationship between the sulfide concentration and the electrochemical performance of $CuCo_2S_4$, CV tests were conducted. From Figure 6a, it can be seen that the curve shapes are roughly the same, and all three samples have a pair of distinct reduction peaks and oxidation peaks; their oxidation and reduction peaks are approximate, manifesting that the $CuCo_2S_4$ electrode has good pseudocapacitance characteristics and electrochemical reversibility. The sample $CuCo_2S_4$-6M has the maximum area of the closed interval, indicating a higher specific capacitance. Figure 6b shows the GCD comparison of $CuCo_2S_4$ at 1 A g^{-1}. Unlike the triangles in the electrodes of the double-layer capacitor, all the samples have a clear plateau region in the 0.2–0.4 potential interval, which further proves that the $CuCo_2S_4$ electrode is a battery-type material. And at the same current density, $CuCo_2S_4$-6M has a longer discharge time, indicating that it has a larger electric capacity. Figure 6c displays Nyquist plots of $CuCo_2S_4$. The equivalent circuit composed of equivalent series resistance (R_S), double-layer capacitance (C_{dl}), Warburg impedor (W), Faraday capacitance (C_F), and charge transfer resistance (R_{ct}) is shown in Figure S3. It is clear that $CuCo_2S_4$-6M shows an almost negligible semicircle and a smallest real axis intercept, demonstrating R_S and R_{ct}. From the tests in Figure 6a–c, it is clear that the $CuCo_2S_4$-6M electrode has superior electrochemical performance. Therefore, the impact of vulcanization time on the electrode material properties was further explored by GCD, CV, and EIS in Figure 6d–f, while maintaining the optimal vulcanization concentration. Figure 6d shows the CV curves obtained at 50 mV s^{-1}, illustrating that $CuCo_2S_4$-6h owns a larger area of the closed interval. Figure 6e displays the GCD curve at the same current density, revealing specific capacitances of 998.2, 1415.6, and 1172.3 F g^{-1} for $CuCo_2S_4$-4h, $CuCo_2S_4$-6h, and $CuCo_2S_4$-8h, respectively. Notably, $CuCo_2S_4$-6h owns the largest specific capacity, which may be attributed to the optimal maintenance of its flower-like hierarchical nanostructure achieved by an appropriate sulfidation time. The electrochemical kinetics were further characterized by EIS (Figure 6f),

demonstrating that $CuCo_2S_4$-6h exhibits the smallest R_{ct} and R_s indicative of faster charge transfer and better electrochemical performance. To further highlight the excellent electrochemical performance of $CuCo_2S_4$-6h, CV tests were performed at different scan rates (Figure 6g). Remarkably, the CV curves remain relatively unchanged even at high scan rates, attributable to the low polarization resistance and good reversibility of $CuCo_2S_4$-6h. The redox reaction can be described by the following equations [46]:

$$CuCo_2S_4 + OH^- + H_2O \leftrightarrow CuSOH + 2CuSOH + e^- \quad (4)$$

$$CoSOH + OH^- \leftrightarrow CoSO + H_2O + e^- \quad (5)$$

$$CuSOH + OH^- \leftrightarrow CuSO + H_2O + e^- \quad (6)$$

In Figure 6h, the specific capacitances of the $CuCo_2S_4$ were calculated to be 1415.6, 1398.5, 1362.8, 1315.1, 1257.3, and 1198.2 F g^{-1} for 1–10 A g^{-1}, and have a charging and discharging plateau, which is consistent with CV results in Figure 6g. The specific capacitance retention at 10 A g^{-1} compared to 1 A g^{-1} is 84.6%, proving its excellent multiplicity performance. Figure 6i displays the cyclic charge/discharge test of $CuCo_2S_4$-6h. After 10,000 cycle tests, the capacity of $CuCo_2S_4$-6h was 91.9% of the initial capacity, which further proves that the $CuCo_2S_4$ nanoflower electrode synthesized under optimized reaction conditions possesses excellent cycling stability.

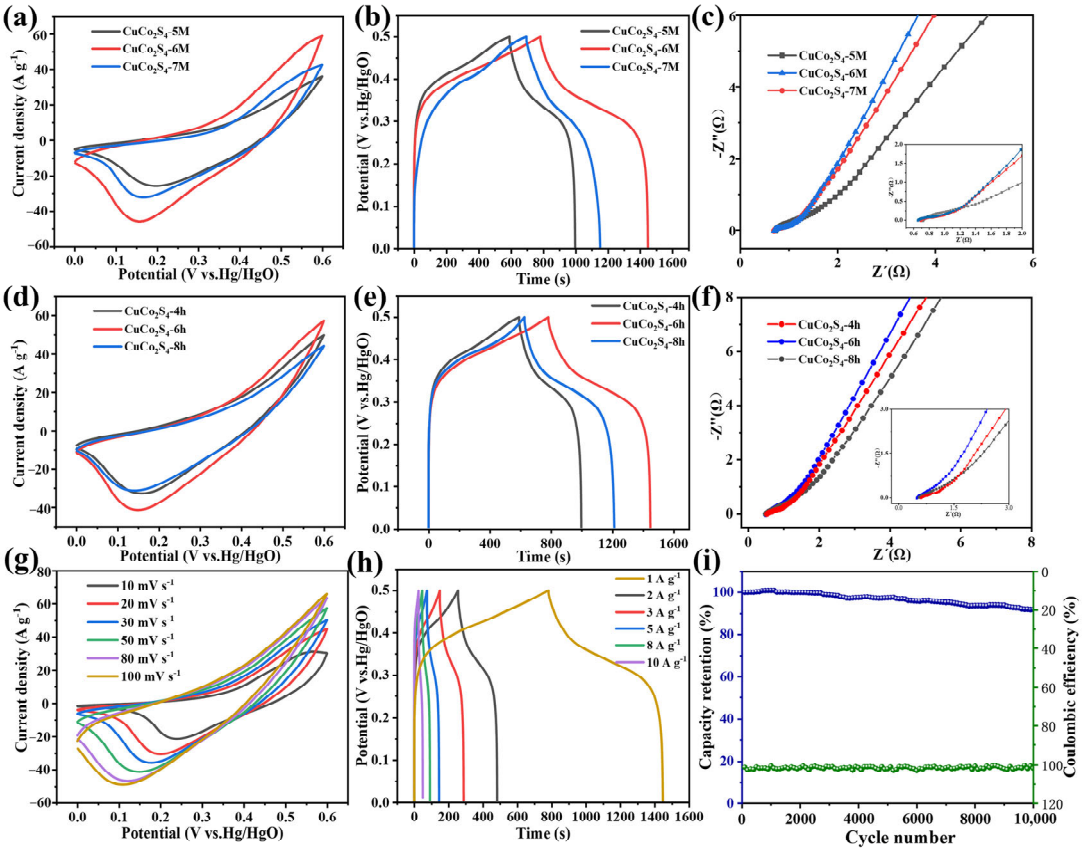

Figure 6. $CuCo_2S_4$-5M, $CuCo_2S_4$-6M, and $CuCo_2S_4$-7M (**a**) CV curves at 50 mV s^{-1}; (**b**) GCD curves at 1 A g^{-1}; (**c**) EIS curves; $CuCo_2S_4$-4h, $CuCo_2S_4$-6h, and $CuCo_2S_4$-8h (**d**) CV curves at 50 mV s^{-1}; (**e**) GCD curves at 1 A g^{-1}; (**f**) EIS curves; (**g**) CV curve and (**h**) GCD curve of $CuCo_2S_4$-6h; (**i**) Cycling properties of $CuCo_2S_4$-6h. The blue line represents capacity retention and corresponds to the blue vertical axis. The green line represents Coulombic efficiency, corresponding to the green vertical axis.

For an analysis of the charge storage behavior of $CuCo_2S_4$ and to determine whether it is surface-controlled battery behavior or capacitance-controlled during the charge and

discharge process, a CV test on $CuCo_2S_4$ was conducted at small scan rates (Figure 7a); the peak data were then fitted to obtain the b value. The relevant calculation formulas are as follows [47–49]:

$$i = a \times v^b \tag{7}$$

$$i(V) = k_1 \times v + k_2 \times v^{1/2} \tag{8}$$

where IP is the peaks current, a and b are the constants, k_1v represents the surface contribution, $K_2V^{\frac{1}{2}}$ represents the diffusion contribution, and b is the slope of the straight line in Figure 7b, which is closely related to different electrochemical behaviors. When b = 1, surface control presents capacitive behavior, whereas when b = 0.5, diffusion control presents battery behavior. For the $CuCo_2S_4$ electrode, b values of 0.78 and 0.81 can be obtained from the calculations, indicating that the surface capacitance and diffusion control exist simultaneously, with the b value being close to 1. Thus, its contribution was fitted and analyzed by Equations (7) and (8). From Figure 7c, it can be observed that the surface control accounts for 82.56%, 84.36%, 85.63%, 87.46%, and 89.27% of the total capacitance as the rate increases. Additionally, the surface-controlled capacitance contribution increases with the scan rate, indicating that the electrode is dominated by capacitive behavior during the electrochemical reactions.

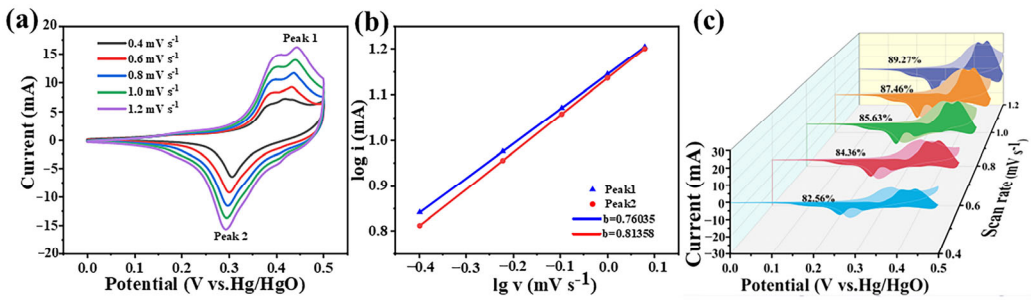

Figure 7. (**a**) CV curves of $CuCo_2S_4$-6h at low scan rates, (**b**) log i and log v curves of $CuCo_2S_4$-6h, (**c**) contribution ratios of diffusion-controlled capacities and capacitive of $CuCo_2S_4$-6h at different scan rates.

To further evaluate the practicality of the ASC device, we assembled a two-electrode supercapacitor with $CuCo_2S_4$ as the positive electrode and RGO as the negative electrode in 2 mol L^{-1} KOH electrolyte. Figure 8a shows the CV curves of the RGO at 10–100 mV s^{-1}, where the quasi-rectangular shape of the bilayer capacitance behavior can be clearly seen. The GCD curves of RGO at 1–10 A g^{-1} (Figure 8b) show a clear, distinct symmetric triangle, indicating high reversibility. Meanwhile, the CV curves for the two electrodes RGO (−1–0 V) and $CuCo_2S_4$ (0–0.6 V) were tested in a three-electrode system at 50 mV s^{-1} (Figure 8c).

Figure 9a shows the schematic diagram of ASC assembled by $CuCo_2S_4$//RGO. In order to determine the most suitable operating voltage range, we performed CV tests at 50 mV s^{-1} (Figure 9b). It is seen that there is no significant change in the curve until the voltage window reaches 0–1.7 V, where a significant polarization occurs. This indicates that the ASC has a stable voltage window at 1.6 V [50]. The CV curve of ASC is shown in Figure 9c. As the sweep speed increases, the area around the CV curve expands, showing good capacitive behavior and multiplier performance. The specific capacitances of $CuCo_2S_4$//RGO were 228.1, 198.3, 183.6, 163.6, 146.2, and 141.5 F g^{-1} at 1–10 A g^{-1} (Figure 9d). Figure 9e shows the Ragone diagram of $CuCo_2S_4$//RGO, which demonstrates that the $CuCo_2S_4$//RGO device has a high power density (812.1 W kg^{-1}) and energy density (61.8 Wh kg^{-1}), which outperforms many copper–cobalt-based supercapacitors (Table S1) [35,51–54]. This indicates that the energy density of the ASC device is well maintained. The $CuCo_2S_4$//RGO device exhibits excellent stability, maintaining a specific capacitance of 82.8% after 10,000 cycle measurements at a high current density of 10 A g^{-1} (Figure 9f).

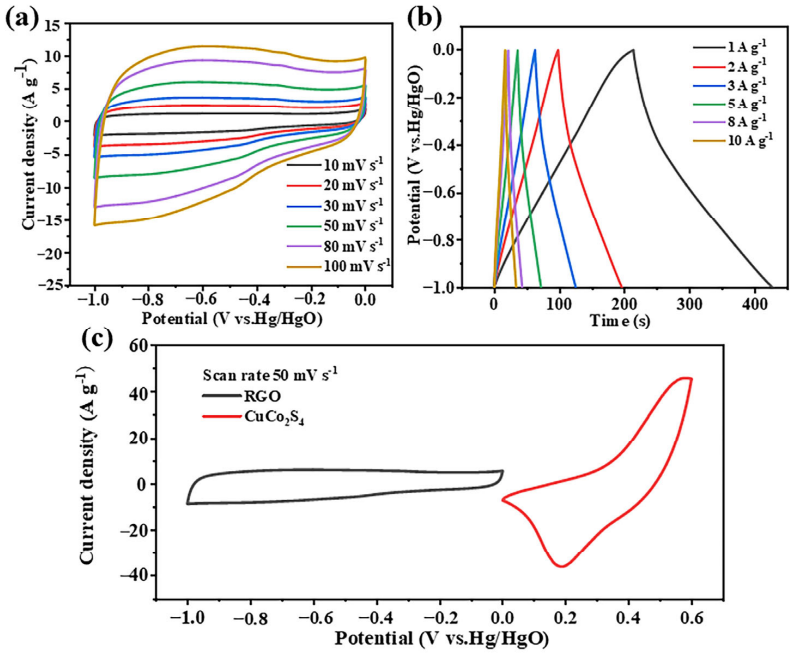

Figure 8. (**a**) CV curves of RGO, (**b**) GCD curves of RGO, (**c**) CV curves of the anode and cathode at 50 mV s^{-1}.

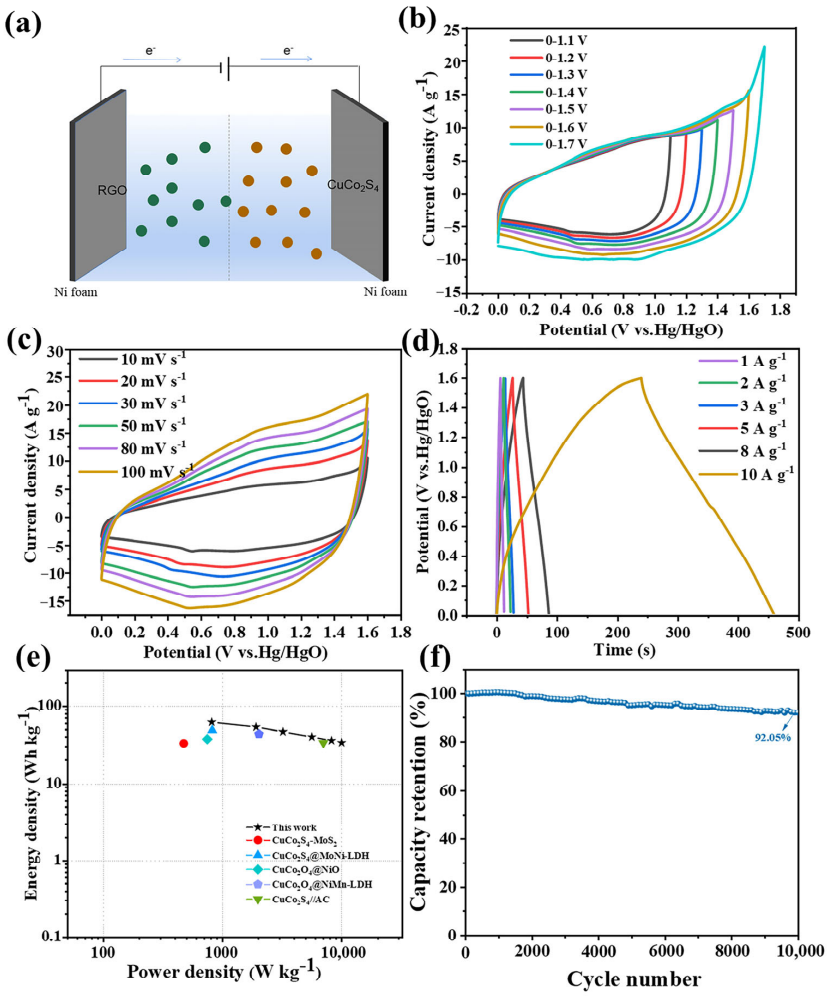

Figure 9. $CuCo_2S_4$-6h//RGO: (**a**) Schematic diagram of an ASC, (**b**) CV curves at different potential ranges, (**c**) CV curves, (**d**) GCD curves, (**e**) Ragone plot, and (**f**) cyclic stability.

4. Conclusions

In summary, a flower-like layered $CuCo_2S_4$ nanostructure was obtained by a two-step solvent–thermal method. Remarkably, the unique hierarchical structure of the $CuCo_2S_4$ electrodes exhibit superior cycle stability (high capacitance retention of 91.90% after 10,000 cycles at high currents) and excellent energy storage performance (1425.6 F g^{-1} at 1 A g^{-1}). In addition, ASC devices have a voltage range of 0–1.6 V and offer power density (812.1 W kg^{-1}) and energy density (61.8 Wh kg^{-1}). The device offers excellent stability, with 92.05% capacity maintenance after 10,000 cycles. Its good cycling stability is attributed to the good electrochemical properties and special nanostructure of $CuCo_2S_4$. Therefore, this paper offers an effective and practical strategy for elaborate nanostructure design and enhancement of supercapacitors' performance.

Supplementary Materials: The following supporting information can be downloaded at: https://www.mdpi.com/article/10.3390/met14020145/s1, Figure S1: (a) XRD patterns of Cu-CCO, (b) Infrared spectra of Cu-CCO samples; Figure S2: SEM images of Cu-CCO precursor nanosheet arrays; Figure S3: Equivalent circuit for three-electrode configuration cell; Figure S4: CV and GCD tests at different sulfide concentrations: (a,b) $CuCo_2S_4$-5M; (c,d) $CuCo_2S_4$-7M; Figure S5: CV and GCD tests with different vulcanization times: (a,b) 4 h; (c,d) 8 h; Figure S6: Cycling performance of $CuCo_2S_4$ electrodes with (a) different sulfide concentrations and (b) different vulcanization times after 10,000 cycles at 10 A g^{-1}; Table S1: Performance comparison of similar materials.

Author Contributions: Conceptualization, M.L. and F.W.; methodology, M.L. and F.W.; validation, W.W. and L.X.; formal analysis, M.L. and N.Y.; investigation, Y.S. and J.Q.; data curation, N.Y., W.W. and L.X.; writing—original draft preparation, M.L.; writing—review and editing, F.W. and J.Q.; supervision, F.W.; project administration, Y.S. All authors have read and agreed to the published version of the manuscript.

Funding: This work is supported by Xuzhou Municipal Government, Grant No. KC21082, acronyms (Xuzhou, China) (KC21082).

Data Availability Statement: Data are contained within the article and Supplementary Materials.

Acknowledgments: This work was supported by resources from Qingqing Yan and Song Wang.

Conflicts of Interest: Authors Fuxiang Wei and Yanwei Sui were employed by the company Jiangsu Huaihai New Energy Co., Ltd. The remaining authors declare that the re-search was conducted in the absence of any commercial or financial relationships that could be construed as a potential conflict of interest.

References

1. Yougbaré, S.; Chou, H.; Yang, C.; Krisnawati, D.I.; Jazidie, A.; Nuh, M.; Kuo, T. Facet-dependent gold nanocrystals for effective photothermal killing of bacteria. *J. Hazard. Mater.* **2021**, *407*, 124617. [CrossRef]
2. Okoro, G.; Husain, S.; Saukani, M.; Mutalik, C.; Yougbaré, S.; Hsiao, Y.; Kuo, T. Emerging Trends in Nanomaterials for Photosynthetic Biohybrid Systems. *ACS Mater. Lett.* **2023**, *5*, 95–115. [CrossRef]
3. Mutalik, C.; Okoro, G.; Krisnawati, D.I.; Jazidie, A.; Rahmawati, E.Q.; Rahayu, D.; Hsu, W.; Kuo, T. Copper sulfide with morphology-dependent photodynamic and photothermal antibacterial activities. *J. Colloid Interface Sci.* **2022**, *607*, 1825–1835. [CrossRef]
4. Mutalik, C.; Okoro, G.; Chou, H.; Lin, I.; Yougbaré, S.; Chang, C.; Kuo, T. Phase-Dependent 1T/2H-MoS_2 Nanosheets for Effective Photothermal Killing of Bacteria. *ACS Sustain. Chem. Eng.* **2022**, *10*, 8949–8957. [CrossRef]
5. Gao, Q.; Wang, J.; Wang, J. Morphology-controllable synthesis of $CuCo_2O_4$ arrays on Ni foam as advanced electrodes for supercapacitors. *J. Alloys Compd.* **2019**, *789*, 193–200. [CrossRef]
6. Zhang, X.; Zhao, Q.; Ma, T.; Li, Z.; Tan, X.; Bateer, B. Design of thin-layer porous nickel cobalt sulfide for high-performance asymmetric supercapacitors. *J. Alloys Compd.* **2023**, *945*, 168902. [CrossRef]
7. Wang, Y.; Huang, X.; Yu, X.; Chen, X.; Jiang, J.; Han, S. Sponge-like 3D flower-like core-shell heterostructure $CuCo_2O_4$@$CuCo_2S_4$ as advanced electrodes for high-performance supercapacitor. *J. Power Sources* **2022**, *551*, 232186. [CrossRef]
8. Wang, Y.; Song, Y.; Xia, Y. Electrochemical capacitors: Mechanism, materials, systems, characterization and applications. *Chem. Soc. Rev.* **2016**, *45*, 5925–5950. [CrossRef]
9. Wu, X.; Meng, L.; Wang, Q.; Zhang, W.; Wang, Y. High flexibility and large energy density asymmetric fibered-supercapacitor based on unique $NiCo_2O_4$@MnO_2 core-shell nanobrush arrays electrode. *Electrochim. Acta* **2019**, *295*, 532–539. [CrossRef]

10. Hussain, I.; Mohapatra, D.; Dhakal, G.; Lamiel, C.; Mohamed, S.G.; Sayed, M.S.; Lee, Y.R.; Lee, J.; Lee, M.; Shim, J. Growth of 2D nanoflakes from 1D long leaf arrays: Electrochemical influence of copper and nickel co-substituted cobalt oxide. *J. Energy Storage* **2020**, *32*, 101871. [CrossRef]
11. Feng, Y.; Liu, W.; Wang, Y.; Gao, W.; Li, J.; Liu, K.; Wang, X.; Jiang, J. Oxygen vacancies enhance supercapacitive performance of $CuCo_2O_4$ in high-energy-density asymmetric supercapacitors. *J. Power Sources* **2020**, *458*, 228005. [CrossRef]
12. Fang, Y.; Yu, X.; Lou, X.W.D. Nanostructured Electrode Materials for Advanced Sodium-Ion Batteries. *Matter* **2019**, *1*, 90–114. [CrossRef]
13. Khedulkar, A.P.; Yu, W.; Dang, V.D.; Pandit, B.; Doong, R. Boosting supercapacitor performance with a cobalt hydroxide in-situ prepara-tion orange peel biochar flower-like composite. *J. Energy Storage* **2024**, *81*, 110302. [CrossRef]
14. Saleki, F.; Mohammadi, A.; Moosavifard, S.E.; Hafizi, A.; Rahimpour, M.R. MOF assistance synthesis of nanoporous double-shelled $CuCo_2O_4$ hollow spheres for hybrid supercapacitors. *J. Colloid Interface* **2019**, *556*, 83–91. [CrossRef]
15. Abo El-Reesh, G.Y.; Farghali, A.A.; Taha, M.; Mahmoud, R.K. Novel synthesis of Ni/Fe layered double hydroxides using urea and glycerol and their enhanced adsorption behavior for Cr(VI) removal. *Sci. Rep.* **2020**, *10*, 587. [CrossRef]
16. Bandyopadhyay, P.; Saeed, G.; Kim, N.H.; Lee, J.H. Zinc-nickel-cobalt oxide@$NiMoO_4$ core-shell nanowire/nanosheet arrays for solid state asymmetric supercapacitors. *Chem. Eng. J.* **2020**, *384*, 123357. [CrossRef]
17. Wang, M.; Yang, J.; Jia, K.; Liu, S.; Hu, C.; Qiu, J. Boosting supercapacitor performance of graphene by coupling with nitrogen-doped hollow carbon frameworks. *Chem. Eur. J.* **2020**, *26*, 2897–2903. [CrossRef]
18. Shao, Y.; Wang, Y.; Zhang, Q.; Li, Y. High-performance flexible asymmetric supercapacitors based on 3D porous graphene/MnO_2 nanorod and graphene/Ag hybrid thin-film electrodes. *J. Mater. Chem. C* **2013**, *1*, 1245–1251. [CrossRef]
19. Wen, P.; Fan, M.; Yang, D.; Wang, Y.; Cheng, H.; Wang, J. An asymmetric supercapacitor with ultrahigh energy density based on nickle cobalt sulfide nanocluster anchoring multi-wall carbon nanotubes hybrid. *J. Power Sources* **2016**, *320*, 28–36. [CrossRef]
20. Lu, Y.; Zhang, Z.; Liu, X.; Wang, W.; Peng, T.; Guo, P.; Sun, H.; Yan, H.; Luo, Y. $NiCo_2S_4$/carbon nanotube nanocomposites with a chain-like architecture for enhanced supercapacitor performance. *CrystEngComm* **2016**, *18*, 7696–7706. [CrossRef]
21. Dakshana, M.; Meyvel, S.; Malarvizhi, M.; Sathya, P.; Ramesh, R.; Prabhu, S.; Silambarasan, M. Facile synthesis of $CuCo_2S_4$ nanoparticles as a faradaic electrode for high performance supercapacitor applications. *Vacuum* **2020**, *174*, 109218. [CrossRef]
22. Cheng, S.; Shi, T.; Chen, C.; Zhong, Y.; Huang, Y.; Tao, X.; Li, J.; Liao, G.; Tang, Z. Construction of porous $CuCo_2S_4$ nanorod arrays via anion exchange for high-performance asymmetric supercapacitor. *Sci. Rep.* **2017**, *7*, 6681. [CrossRef]
23. Li, Q.; Lu, W.; Li, Z.; Ning, J.; Zhong, Y.; Hu, Y. Hierarchical MoS_2/$NiCo_2S_4$@C urchin-like hollow microspheres for asymmetric supercapacitors. *Chem. Eng. J.* **2020**, *380*, 122544. [CrossRef]
24. Li, H.; Yang, H.; Sun, Z.; Shi, Y.; Cheng, H.; Li, F. A highly reversible Co3S4 microsphere cathode material for aluminum-ion batteries. *Nano Energy* **2019**, *56*, 100–108. [CrossRef]
25. Bahaa, A.; Balamurugan, J.; Kim, N.H.; Lee, J.H. Metal-organic framework derived hierarchical copper cobalt sulfide nanosheet arrays for high-performance solid-state asymmetric supercapacitors. *J. Mater. Chem. A* **2019**, *7*, 8620–8632. [CrossRef]
26. Liu, S.; Jun, S.C. Hierarchical manganese cobalt sulfide core-shell nanostructures for high-performance asymmetric supercapacitors. *J. Power Sources* **2017**, *342*, 629–637. [CrossRef]
27. Shen, L.; Yu, L.; Wu, H.; Yu, X.; Zhang, X.; Lou, X. Formation of nickel cobalt sulfide ball-in-ball hollow spheres with enhanced electrochemical pseudocapacitive properties. *Nat. Commun.* **2015**, *6*, 6694. [CrossRef]
28. Liu, S.; San Hui, K.; Hui, K.N.; Yun, J.M.; Kim, K.H. Vertically stacked bilayer $CuCo_2O_4$/$MnCo_2O_4$ heterostructures on functionalized graphite paper for high-performance electrochemical capacitors. *J. Mater. Chem. A* **2016**, *4*, 8061–8071. [CrossRef]
29. Kang, L.; Huang, C.; Zhang, J.; Zhang, M.; Zhang, N.; Liu, S.; Ye, Y.; Luo, C.; Gong, Z.; Wang, C.; et al. Effect of fluorine doping and sulfur vacancies of $CuCo_2S_4$ on its electrochemical performance in supercapacitors. *Chem. Eng. J.* **2020**, *390*, 124643. [CrossRef]
30. Xu, X.; Liu, Y.; Dong, P.; Ajayan, P.M.; Shen, J.; Ye, M. Mesostructured $CuCo_2S_4$/$CuCo_2O_4$ nanoflowers as advanced electrodes for asymmetric supercapacitors. *J. Power Sources* **2018**, *400*, 96–103. [CrossRef]
31. Li, H.; Li, Z.; Wu, Z.; Sun, M.; Han, S.; Cai, C.; Shen, W.; Liu, X.; Fu, Y. Enhanced electrochemical performance of $CuCo_2S_4$/carbon nanotubes composite as electrode material for supercapacitors. *J. Colloid Interface Sci.* **2019**, *549*, 105–113. [CrossRef]
32. Wang, P.; Zhang, Y.; Yin, Y.; Fan, L.; Zhang, N.; Sun, K. In Situ Synthesis of $CuCo_2S_4$ @N/S-Doped Graphene Composites with Pseudocapacitive Properties for High-Performance Lithium-Ion Batteries. *ACS Appl. Mater. Interfaces* **2018**, *10*, 11708–11714. [CrossRef]
33. Jia, H.; Cai, Y.; Wang, Z.; Zheng, X.; Li, H.; Liang, H.; Qi, J.; Cao, J.; Feng, J.; Fei, W. Sea urchin-like $CuCo_2S_4$ microspheres with a controllable interior structure as advanced electrode materials for high-performance supercapacitors. *Inorg. Chem. Front.* **2020**, *7*, 603–609. [CrossRef]
34. Tang, J.; Ge, Y.; Shen, J.; Ye, M. Facile synthesis of $CuCo_2S_4$ as a novel electrode material for ultrahigh supercapacitor performance. *Chem. Commun.* **2020**, *52*, 1509–1512. [CrossRef]
35. Zhang, K.; Zeng, H.; Li, H.; Xu, S.; Lv, S.; Wang, M. Controllable preparation of $CuCo_2S_4$ nanotube arrays for high-performance hybrid supercapacitors. *Electrochim. Acta* **2022**, *404*, 139681. [CrossRef]
36. Fan, L.; Pan, F.; Tu, Q.; Gu, Y.; Huang, J.; Huang, Y.; Wu, J. Synthesis of $CuCo_2S_4$ nanosheet arrays on Ni foam as binder-free electrode for asymmetric supercapacitor. *Int. J. Hydrogen Energy* **2018**, *43*, 23372–23381. [CrossRef]
37. Wang, Y.; Yang, D.; Zhou, T.; Pan, J.; Wei, T.; Sun, Y. Oriented $CuCo_2S_4$ nanograss arrays/Ni foam as an electrode for a high-performance all-solid-state supercapacitor. *Nanotechnology* **2020**, *28*, 465402. [CrossRef]

38. Tsai, M.; Chen, T.; Juang, Y.; Hua, L.; Huang, C. High catalytic performance of CuCo/nickel foam electrode for ammonia electrooxidation. *Electrochem. Commun.* **2020**, *121*, 106875. [CrossRef]
39. Guan, B.; Zhao, Y.; Zhang, N.; Zhang, J.; Sun, T.; Yi, T. Highly uniform platanus fruit-like $CuCo_2S_4$ microspheres as an electrode material for high performance lithium-ion batteries and supercapacitors. *Dalton T* **2021**, *50*, 13042–13051. [CrossRef]
40. Han, L.; Liu, X.; Cui, Z.; Hua, Y.; Wang, C.; Zhao, X.; Liu, X. Hierarchical copper cobalt sulfide nanobelt arrays for high performance asymmetric supercapacitors. *Inorg. Chem. Front.* **2021**, *8*, 325–336. [CrossRef]
41. Mane, S.M.; Teli, A.M.; Yang, H.K.; Kwon, E.; Nimbalkar, N.A.; Patil, D.R.; Shin, J.C. Nanoneedles anchored ultrathin petals of CuCo layered double hydroxide with high areal capacitance and long cycle life for high-performance hybrid supercapacitors. *J. Energy Storage* **2023**, *62*, 106941. [CrossRef]
42. Kumar, L.; Boruah, P.K.; Borthakur, S.; Saikia, L.; Das, M.R.; Deka, S. CuCo-Layered Double Hydroxide Nanosheet-Based Polyhedrons for Flexible Supercapacitor Cells. *ACS Appl. Nano Mater.* **2021**, *4*, 5250–5262. [CrossRef]
43. Sun, P.; Zhang, J.; Huang, J.; Wang, L.; Wang, P.; Cai, C.; Lu, M.; Yao, Z.; Yang, Y. Bimetallic MOF-derived (CuCo)Se nanoparticles embedded in nitrogen-doped carbon framework with boosted electrochemical performance for hybrid supercapacitor. *Mater. Res. Bull.* **2021**, *137*, 111196. [CrossRef]
44. Du, J.; Yan, Q.; Li, Y.; Cheng, K.; Ye, K.; Zhu, K.; Yan, J.; Cao, D.; Zhang, X.; Wang, G. Hierarchical copper cobalt sulfides nanowire arrays for high-performance asymmetric supercapacitors. *Appl. Surf. Sci.* **2019**, *487*, 198–205. [CrossRef]
45. Tang, N.; You, H.; Li, M.; Chen, G.Z.; Zhang, L. Cross-linked $Ni(OH)_2/CuCo_2S_4/Ni$ networks as binder-free electrodes for high performance supercapatteries. *Nanoscale* **2018**, *10*, 20526–20532. [CrossRef]
46. You, H.; Zhang, L.; Jiang, Y.; Shao, T.; Li, M.; Gong, J. Bubble-supported engineering of hierarchical $CuCo_2S_4$ hollow spheres for enhanced electrochemical performance. *J. Mater. Chem. A* **2018**, *6*, 5265–5270. [CrossRef]
47. Chu, X.; Meng, F.; Yang, H.; Zhang, W.; Qin, T.; Wang, Z.; Molin, S.; Jasinski, P.; Zheng, W. Cu-Doped Layered Double Hydroxide Constructs the Performance-Enhanced Supercapacitor Via Band Gap Reduction and Defect Triggering. *ACS Appl. Energy Mater.* **2022**, *5*, 2192–2201. [CrossRef]
48. Yuan, J.; Li, Y.; Lu, G. Controlled Synthesis of Flower-like Hierarchical NiCo-Layered Double Hydroxide Integrated with Metal-Organic Framework-Derived Co@C for Supercapacitors. *ACS Appl. Mater. Interface* **2023**, *15*, 36143–36153. [CrossRef]
49. Du, X.; Su, H.; Zhang, X. Metal-Organic Framework-Derived Cu-Doped Co_9S_8 Nanorod Array with Less Low-Valence Co Sites as Highly Efficient Bifunctional Electrodes for Overall Water Splitting. *ACS Sustain. Chem. Eng.* **2019**, *7*, 16917–16926. [CrossRef]
50. Peng, H.; Wei, C.; Wang, K.; Meng, T.; Ma, G.; Lei, Z.; Gong, X. $Ni_{0.85}Se@MoSe_2$ Nanosheet Arrays as the Electrode for High-Performance Supercapacitors. *ACS Appl. Mater. Interface* **2017**, *9*, 17067–17075. [CrossRef]
51. Hasan, S.; Reaz, A.H.; Das, S.; Roy, C.K.; Basith, M.A. $CuCo_2S_4$-MoS_2 nanocomposite: A novel electrode for high-performance supercapacitors. *J. Mater. Chem. C* **2022**, *10*, 7980–7996. [CrossRef]
52. Zhang, C.; Sui, Q.; Lu, L.; Zou, Y.; Xu, F.; Sun, L.; Cai, D.; Xiang, C. Hollow core–shell $CuCo_2O_4$@MoNi-layered double hydroxides as an electrode material for supercapacitors. *J. Energy Storage* **2023**, *61*, 106691. [CrossRef]
53. Zhao, W.; Xu, X.; Wu, N.; Zhao, X.; Gong, J. Dandelion-like $CuCo_2O_4$@ NiMn LDH Core/Shell Nanoflowers for Excellent Battery-Type Supercapacitor. *Nanomaterials* **2023**, *13*, 730. [CrossRef] [PubMed]
54. Xu, K.; Ma, S.; Shen, Y.; Ren, Q.; Yang, J.; Chen, X.; Hu, J. $CuCo_2O_4$ nanowire arrays wrapped in metal oxide nanosheets as hierarchical multicomponent electrodes for supercapacitors. *Chem. Eng. J.* **2019**, *369*, 363–369. [CrossRef]